Applied Physics Letters

# Identifying the octupole antiferromagnetic domain orientation in $Mn_3NiN$ by scanning anomalous Nernst effect microscopy

Cite as: Appl. Phys. Lett. **120**, 232402 (2022); https://doi.org/10.1063/5.0091257
Submitted: 13 March 2022 • Accepted: 19 May 2022 • Published Online: 08 June 2022
Published open access through an agreement with Imperial College London

F. Johnson, J. Kimák, J. Zemen, et al.



Applied Physics Letters ARTICLE scitation.org/journal/apl

# Identifying the octupole antiferromagnetic domain orientation in $Mn_3NiN$ by scanning anomalous Nernst effect microscopy

Cite as: Appl. Phys. Lett. **120**, 232402 (2022); doi: 10.1063/5.0091257
Submitted: 13 March 2022 · Accepted: 19 May 2022 ·
Published Online: 8 June 2022



F. Johnson,[1,a)] J. Kimák,[2,a)] J. Zemen,[3] Z. Šobáň,[4] E. Schmoranzerová,[2] J. Godinho,[2,4] P. Němec,[2] S. Beckert,[5] H. Reichlová,[4,5] D. Boldrin,[1,6] J. Wunderlich,[7] and L. F. Cohen[1]

## AFFILIATIONS

[1]Blackett Laboratory, Imperial College, Prince Consort Rd., London SW7 2AZ, United Kingdom
[2]Faculty of Mathematics and Physics, Charles University, Prague 121 16, Czech Republic
[3]Faculty of Electrical Engineering, Czech Technical University, Technicka 2, Prague 166 27, Czech Republic
[4]Institute of Physics, Czech Academy of Sciences, Prague 181 21, Czech Republic
[5]Institut für Festkörper- und Materialphysik, Technische Universität Dresden, 01062 Dresden, Germany
[6]SUPA, School of Physics and Astronomy, University of Glasgow, Glasgow G12 8QQ, United Kingdom
[7]Institute of Experimental and Applied Physics, University of Regensburg, 93051 Regensburg, Germany

[a)]**Authors to whom correspondence should be addressed:** fj214@ic.ac.uk and jozef.kimak@mff.cuni.cz

## ABSTRACT

The intrinsic anomalous Nernst effect in a magnetic material is governed by the Berry curvature at the Fermi energy and can be realized in non-collinear antiferromagnets with vanishing magnetization. Thin films of (001)-oriented $Mn_3NiN$ have their chiral antiferromagnetic structure located in the (111) plane facilitating the anomalous Nernst effect unusually in two orthogonal in-plane directions. The sign of each component of the anomalous Nernst effect is determined by the local antiferromagnetic domain state. In this work, a temperature gradient is induced in a 50 nm thick $Mn_3NiN$ two micrometer-size Hall cross by a focused scanning laser beam, and the spatial distribution of the anomalous Nernst voltage is used to image and identify the octupole macrodomain arrangement. Although the focused laser beam width may span many individual domains, cooling from room temperature to the antiferromagnetic transition temperature in an in-plane magnetic field prepares the domain state, producing a checkerboard pattern resulting from the convolution of contributions from each domain. These images together with atomistic and micromagnetic simulations suggest an average macrodomain of the order of 1 $\mu m^2$.



For spintronic applications, interest in antiferromagnets has accelerated due to anticipated advantages in speed and energy efficiency they may offer over ferromagnets for memory and logic devices.[1,2] $Mn_3(A,B)N$ and related material families have been shown to support piezomagnetism,[3] giant anomalous Hall effect (AHE),[4] and magneto-optical Kerr effect (MOKE)[5] signatures plus unconventional torque geometries useful for out-of-plane magnetization switching.[6] Understanding and controlling the antiferromagnetic (AFM) domain structure are essential for applications, although challenging to capture because of the compensated, near zero magnetization. By using a scanning laser to generate an out-of-plane thermal gradient, the anomalous Nernst effect (ANE) can be used as a powerful tool to image AFM domains/domain clusters, as previously demonstrated in $Mn_3Sn$,[7] and a similar domain structure has been imaged in the collinear AFM CuMnAs using the magneto-Seebeck effect.[8]

The ANE is one of a number of thermoelectric (TE) effects found in magnetic materials. The different geometries of the various TE effects are illustrated in Fig. 1(a). Commercial TE devices exploit the conventional Seebeck effect, where a thermal gradient applied between two terminals generates a potential difference along the same direction.[9,10] In the Nernst effect (NE), the electric potential is perpendicular to both the applied temperature gradient and the applied magnetic field[11] and is potentially attractive for commercial applications due to simpler thermopile design.[12,13] The anomalous Nernst effect manifests in ferromagnets, takes the same geometry as the NE, and is proportional to magnetization.[14] Originally thought to be present only in

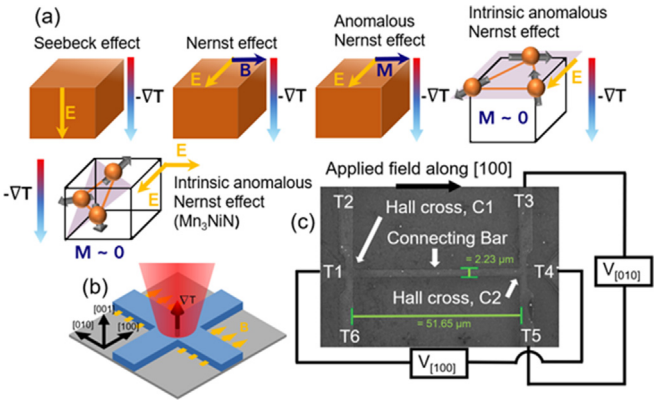


**FIG. 1.** (a) Diagram of the various thermoelectric effects and their respective geometries. (b) Scematic of the scanning anomalous Nernst measurement of the $Mn_3NiN$ Hall cross. The laser is scanned across the surface generating a thermal gradient out-of-plane. The resultant thermovoltage in the two in-plane directions is simultaneously measured. (c) SEM image of the device with overlaid dimensions, contacts T1–T6 and regions of the device labeled, and experimental geometry. $V_{[010]}$ is the conventional component of the anomalous Nernst effect, and $V_{[100]}$ is the unconventional component.

materials with finite magnetization, and it is now accepted that there is an intrinsic ANE component associated with the Berry curvature of the band structure at the Fermi energy.[15] Experimental observation in non-collinear antiferromagnets (AFMs) with vanishing magnetization, such as $Mn_3Sn$,[16–19] has helped cement this understanding. However, the magnitude of the intrinsic ANE in AFMs is found to be modest compared to conventional thermopower.[20,21] Improvement requires manipulation of both the Berry curvature and the Fermi level—unlike the anomalous Hall effect, and maximizing the ANE requires topological features in the band structure to be moved away from the Fermi energy.[22–24] The family of nitride antiperovskites $Mn_3(A,B)N$ is chemically flexible on the A and B sites, facilitating tuning of electronic properties by chemical means.[25] Furthermore, it has recently been predicted that $Mn_3NiN$ presents a giant anomalous Nernst conductivity (ANC),[26] and it has been shown that the Berry curvature in $Mn_3NiN$ is also tunable using strain.[3,27] These directions are as yet embryonic.

Here, we employ the scanning ANE technique to examine the magnetic domain structure in non-collinear cubic antiperovskite $Mn_3NiN$ thin films. $Mn_3NiN$ films of thickness 50 nm used in this study were grown using pulsed laser deposition at 400 °C on single crystal (001)-oriented $SrTiO_3$ (STO) substrates as described in detail in Ref. 3. The films are oriented, such that the [001] crystal direction (c-axis) points out-of-plane, and 2 $\mu$m wide Hall bars patterned by electron-beam lithography are oriented along the [100] crystal direction. A typical device and the experimental geometry are shown in Figs. 1(b) and 1(c), respectively. The out-of-plane thermal gradient was generated by a continuous wave (CW) laser, a power of 10 mW, and a wavelength of $\lambda = 800$ nm and modulated by a mechanical chopper at a frequency of 1.6 kHz. The beam was focused on the sample by an objective lens to a 1.8 $\mu$m diameter beam. The objective lens was placed onto a 3D piezo-positioner, which allows for scanning of the laser spot across the Hall bar with a precision of 10 nm and a step-size of 400 nm. The thermo-voltage was measured using a lock-in amplifier. Simultaneously, the intensity of the reflected light was recorded in order to identify the position of the focused laser beam during the experiment. A schematic of the measurement setup is included in the supplementary material, Fig. S1. The data shown in the paper were taken at 50 K on the right hand cross C2. Supplementary material Fig. S2 shows data taken at 100 K on the left hand cross C1 and in the bar region in Fig. S3.

Atomistic, micromagnetic, and finite element method (FEM) simulations as implemented in the COMSOL Multiphysics® software are used to inform our experiments. The details of these calculations are also included in the supplementary material.

Growth on a STO substrate imparts a small compressive bi-axial in-plane strain of the order of 0.1% (Ref. 3), and the film considered here enters the non-collinear AFM magnetic phase, termed $\Gamma^{4g}$, below the magnetic ordering temperature $T_N = 230$ K.

From the Mott relation between the anomalous Hall conductivity (AHC) and the anomalous Nernst conductivity (ANC),[28–30] it is anticipated that the symmetry of the two effects should be the same. The $\Gamma^{4g}$ phase can be described as a linear combination of three cluster octupole moments, and the magnetic symmetry group is the basis for the non-zero intrinsic anomalous Nernst effect in the material.[31] This phase has eight possible domain arrangements, corresponding to the $\Gamma^{4g}$ spin orientation being located in one of the eight (111) planes, as shown in Fig. 2. Manipulating these domains by an external magnetic field is made

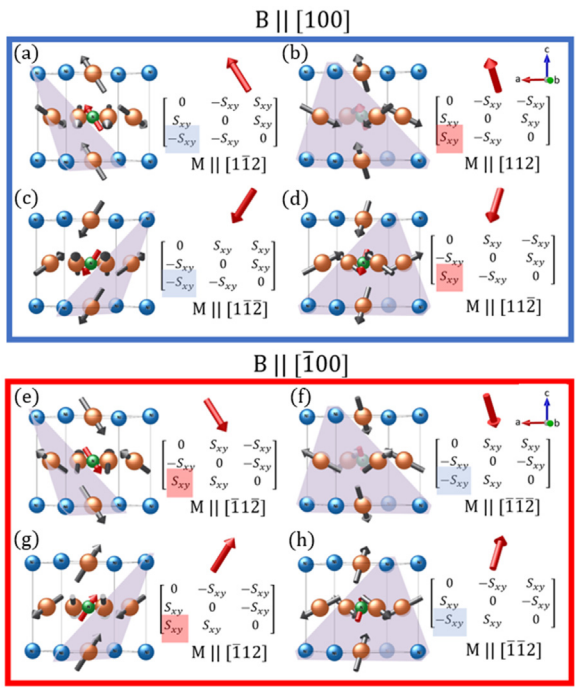


**FIG. 2.** The eight variants of $\Gamma^{4g}$ with the associated anomalous Nernst conductivity tensors and net moment directions. The first four variants in the blue box (a)–(d) are favored when B||[100] and give negative $V_{[010]}$ signal but can give positive or negative $V_{[100]}$. The other four in the red box (e)–(h) are favored for the case B||[$\bar{1}$00], and all have positive $V_{[010]}$ signal but may also have either negative or positive $V_{[100]}$. The coloring of the outer box shows the sign of the conventional Nernst component, while the highlighted component of the anomalous Nernst tensor shows the sign of the unconventional component. Drawings of the variants were produced using Ref. 41.

possible by growth on the STO substrate, where the in-plane strain leads to canting of the local Mn moments, creating a net weak uncompensated moment (red arrow in Fig. 2)—with each one of the eight domains having the moment lie in one of the eight equivalent ⟨112⟩ directions. By cooling the sample in an applied in-plane magnetic field, this weak net moment can be aligned to the field direction, thereby facilitating control and measurement of individual AFM macrodomains.

From the particular symmetries, it follows that the intrinsic ANE is permitted in both in-plane crystal directions [100] and [010] when the out-of-plane thermal gradient, $\nabla T_{[001]}$, is applied to the Hall cross using the focused laser beam. Therefore, by scanning the laser over the device and measuring the sign of the resultant thermo-voltage in these two directions simultaneously, hence referred to as $V_{[100]}$ and $V_{[010]}$, we can identify the arrangement of different macrodomains.

Cooling in magnetic field $B$ ||[100] favors the four variants of $\Gamma^{4g}$ that have the in-plane component of the weak residual magnetic moment aligned to either [110] or [1$\bar{1}$0]—these are Figs. 2(a)–2(d) shown in the blue box. This is because the net moments of these four variants all have the same projection to the applied field. Cooling with $B$ ||[$\bar{1}$00] favors Figs. 2(e)–2(h) shown in the red box. These groups of variants will have identical sign of $V_{[010]}$. This is clearly observed in our measurement presented in Fig. 3. The Hall cross device labeled C2 in Fig. 1(c) is first located and identified using the optical reflected intensity [Figs. 3(a) and 3(b)]. After cooling from 300 to 50 K in a negative (positive) 0.5 T external magnetic field applied in the [100] direction, the region shows a saturated negative (positive) $V_{[010]}$ [Figs. 3(c) and 3(d)]. The signal remains unchanged even after removing the magnetic field. The voltage $V_{[010]}$ has the same geometry of the ANE as measured in a typical ferromagnetic system and, hence, can be considered the "conventional" ANE.

From the signal shown in Fig. 3 alone we cannot distinguish between the four possible variants of micromagnetic domains [Figs. 2(a)–2(d)]. However, by measuring the "unconventional" ANE signal $V_{[100]}$ on the perpendicular set of contacts (Fig. 4), further a magnetic structure can be identified with positive and negative regions ∼1 $\mu$m in diameter arranged in an alternating pattern. This unconventional $V_{[100]}$ response corresponds to the blue and red highlighted components of the anomalous Nernst tensor in Fig. 2. The form of the tensor was derived using the linear response symmetry analysis tool and assuming the Mott formula.[32] The variants with [010] components to their moment [Figs. 2(a), 2(c), 2(f), and 2(h)] produce a positive $V_{[100]}$ signal, while the variants that have [0$\bar{1}$0] components [Figs. 2(b), 2(d), 2(e), and 2(g)] produce a negative signal. The sign of $V_{[010]}$ combined with the sign of $V_{[100]}$, therefore, allows us to identify each region as corresponding to the two variants with an identical in-plane component of the magnetic moment.

From symmetry considerations, it is expected that the magnitude of the unconventional intrinsic ANE and conventional intrinsic ANE components should be comparable, but experimentally, we find the unconventional ANE is approximately six times smaller (see Figs. 3 and 4, respectively). This can be understood by taking into consideration the likely size of the domains. A recent work on other AFM systems using X-ray magnetic linear dichroism photoemission electron microscopy (XMLD-PEEM),[33] nitrogen-vacancy diamond (NVD) magnetometry,[34] or Kerr microscopy[35] has identified individual domains considerably smaller than the feature size shown in Fig. 4. The spatial resolution of the scanning ANE technique is limited by the lateral dimension of the thermally diffused spot on the

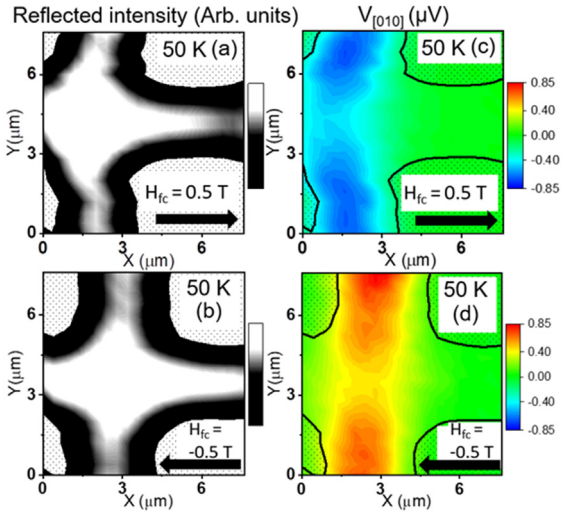


**FIG. 3.** The conventional anomalous Nernst $V_{[010]}$ thermo-voltage in the Hall cross. (a) and (b) The reflected intensity of the area of the device scanned. (c) and (d) The $V_{[010]}$ thermo-voltage scans measured after cooling from 300 to 50 K in positive and negative 0.5 T, respectively, with the device area from the reflected intensity marked by black lines. In these scans, the region appears fully polarized.

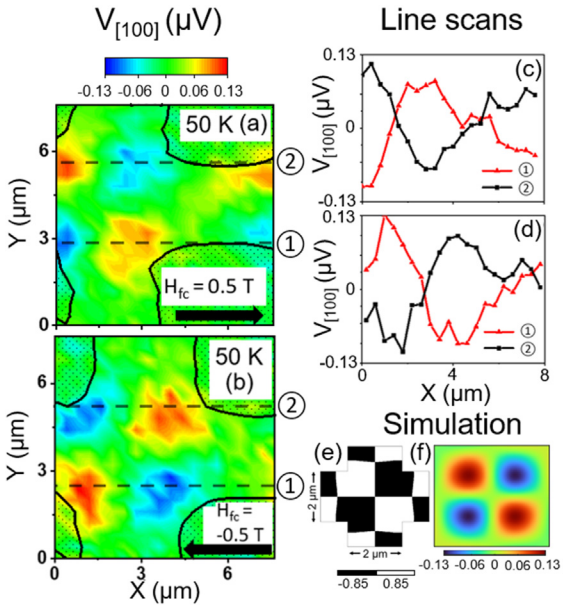


**FIG. 4.** In the corresponding $V_{[100]}$ thermo-voltage scans (a) and (b), further magnetic contrast is visible due to the underlying AFM domain clusters. The red and blue regions correspond to the positive and negative highlighted terms in the anomalous Nernst tensor in Fig. 2. (c) and (d) Line scans taken from the $V_{[100]}$ thermo-voltage scans showing the width of the domain clusters. (e) and (f) Simulated $V_{[100]}$ scan for the checkerboard domain configuration with amplitude ±0.85 $\mu$V [(e) schematic] using Gaussian smoothing with a 1.8 $\mu$m FWHM to account for the focused laser spot. There is an overall amplitude reduction as well as a smoothing of the pattern.

sample, likely to be greater than the CW laser spot itself (1.8 $\mu$m in diameter). The features we observe are due to the convolution of the laser beam as it scans across a mixed domain region with individual domains that contribute positive and negative ANE voltages. This, thus, provides explanation for a reduced magnitude of the overall signal in the unconventional ANE direction compared to the conventional ANE measurement, implying individual domains smaller than the laser spot size. However, were different domain types equally represented and significantly smaller than the spot size, this would result in a zero average ANE signal in the unconventional [100] direction. Clearly, this is not the case, meaning that there are some overriding physical phenomena that encourage a propensity of domains of certain types. We consider four possible explanations: strain, antiferromagnetic domain walls (AFDWs), in-plane heat gradient, and magnetostatics.

Strain from the constrained geometry of the Hall cross could, in principle, be responsible. However, FEM calculations (see the supplementary material for details) of the strain distribution indicate the strain due to lattice mismatch relaxation after patterning of the structure only extends 100 nm from the edges of the device. Therefore, it is likely to play a role only when devices in the order of magnitude smaller than those considered here are made.

In $Mn_3Sn$, it has been suggested that the 180° antiferromagnetic domain wall (AFDW) is approximately 800 nm thick with a Bloch-like structure consisting of three 60° AFDWs but the size and structure of the AFDW in $Mn_3NiN$ are unknown, and it is, therefore, plausible that the $V_{[100]}$ signal could be related to large domain walls.[36] Using atomistic simulations of strained $Mn_3NiN$, alongside prior density functional theory calculations (see the supplementary material for further details), we simulate the 180° domain wall and parameterize it in terms of the strain induced weak ferromagnetic moment.[37] The parameters used in these simulations are summarized in Table I. We also obtain a three-step domain wall, however, with two 45° AFDWs occurring within the first and last steps, and a 90° AFDW within the central step. The width of each domain wall is ∼8 nm, while the length of the full 180° AFDW is ∼50 nm, significantly smaller than in $Mn_3Sn$, suggesting that the AFDWs do not provide a dominant contribution to the $V_{[100]}$ signal.

A further consideration to address for the finite voltage $V_{[100]}$ relates to the ordinary Seebeck due to the in-plane heat gradient $\nabla T_{IP}$, which is present at the edges of the laser spot and points radially outward from the center. When the laser is shone in the top left corner of the Hall cross C2, an in-plane heat gradient may be generated with components toward contacts T4 and T5. When the laser is shone in the bottom right corner, the in-plane heat gradient will point toward contacts T3 and T1. Therefore, if the in-plane heat gradient was large and the ordinary Seebeck effect were visible, we would expect the top left corner and the bottom right corner of C2 to present the opposite sign of voltage in both the $V_{[010]}$ and $V_{[100]}$ scans, as the in-plane heat gradient has reversed sign. Yet, this is not what is observed, in fact both corners show the same sign of voltage. Furthermore, the ordinary Seebeck effect does not change sign in the reversed field, yet the signal we observe shows a change in sign with field. Therefore, the signal cannot be attributed to the ordinary Seebeck. (As shown previously with $Mn_3Sn$,[7] the domain structure may be rewritten if a region of the device is scanned using a higher laser power while a reversed field is applied, see the supplementary material, Fig. S4 and associated text.)

Other effects that may occur in the presence of the in-plane heat gradient are the magneto-Seebeck and the component of anomalous Nernst associated with in-plane thermal gradients. The influence of these is discussed in detail in the supplementary material. For better understanding of the macrodomain structure, we also use FEM simulations to inform about the potential impact of this heat gradient. FEM calculations of heat propagation in the device [see Fig. S5(a) in the supplementary material] indicate this gradient is only significant for an extremely narrow region (of the order of 150 nm) compared to the out-of-plane heat gradient, which is present over the entire laser spot. Its effect cancels when the laser spot is away from the edges of the device because the radially opposing directions of heat gradient generate opposite sign of the ANE voltage.

Although the resultant octupole magnetization is modest, an order of magnitude smaller than typical ferromagnets, the resultant pattern that emerges from the ANE in the unconventional geometry is a checkerboard-type arrangement of domains constricted by the Hall cross with area ∼1 $\mu m^2$ indicative of a significant role of the magnetic dipole–dipole interaction [Figs. 4(a) and 4(b)]. The extracted line scans from these images, which are shown in Figs. 4(c) and 4(d), reveal a gradual change from maxima to minima over the length of the device. Micromagnetic simulation of a film of 50 nm thickness, with parameters taken from the atomistic simulation, yields a checkerboard-type

**TABLE I.** Parameters used in atomistic simulations of strained $Mn_3NiN$ with their origins. $Mn_1$, $Mn_2$, and $Mn_3$ refer to the Mn spins located at (0.5, 0.5, 0), (0.5, 0, 0.5), and (0, 0.5, 0.5), respectively.

| Parameter | Symbol | Value | Origin |
|---|---|---|---|
| Unit cell size | $a$, $b$, $c$ | $a = b = 3.882\,114$ Å, $c = 3.895478$ Å | Ref. 38, 0.1% strained values obtained with Poisson's ratio from Ref. 39. |
| Exchange energy (NN) | $J_{ij}$ $Mn_1$–$Mn_2$, $Mn_3$ | $-4.46 \times 10^{-21}$ J | *Ab initio* calculations to find unstrained values (see the supplementary material) with strain adjustments inferred by fitting atomistic simulation of M(T) to experimental values of $T_N$ from Ref. 39. |
| | $J_{ij}$ $Mn_2$–$Mn_3$ | $-5.16 \times 10^{-21}$ J | |
| Exchange energy (NNN) | $J_{ij}$ Mn−Mn in a, b directions | $5.2 \times 10^{-22}$ J | |
| | $J_{ij}$ Mn–Mn in c directions | $4.8 \times 10^{-22}$ | |
| Uniaxial anisotropy constant | $K$-$Mn_1$ | $2.25 \times 10^{-23}$ J | Ref. 40, adjusted for strain. |
| | $K$-$Mn_2$, $Mn_3$ | $2.55 \times 10^{-23}$ J | |
| Atomic spin moment | $\mu_s$-$Mn_1$ | 2.830 51 $\mu_B$ | *Ab initio* atomistic spin moments calculated for 0.1% strain |
| | $\mu_s$-$Mn_{2,3}$ | 2.824 64 $\mu_B$ | |

arrangement of domains within the Hall cross geometry, with area $\sim 1\ \mu m^2$ [Fig. 4(e)]. If we then simulate the convolution process, taking the checkerboard pattern scanned with a stimulating laser field of 2 $\mu$m size, the resulting detected $V_{ANE}$ signal [Fig. 4(f)] strongly resembles the observed patterns [Figs. 4(a) and 4(b)] and with a reduced signal similarly of magnitude comparable to experiment. In contrast, $V_{[010]}$, the conventional component, is unaffected by the domain distribution because the contribution from all the different possible domain arrangements adds constructively.

In conclusion, we have shown that the non-collinear $Mn_3NiN$ films grown on STO substrates support the ANE, and that by using a scanning laser arrangement, we can unveil the symmetries of the octupole macrodomain structure. We find conventional and unconventional components to the ANE due to the magnetic symmetry of the material. Although the method has proved ideal for spatial investigation of the domain arrangement, rigorous calibration of the temperature gradient would be required to determine the absolute value of the ANE. We note, however, that the raw values are similar to those previously reported for $Mn_3Sn$ films using the same experimental setup.[7] We finally determine that macrodomain clusters, present in the films, can be controlled through the magnetostatics associated with the modest net octupole moment.

See the supplementary material for details of the simulations.

F.J. acknowledges funding from Hitachi Cambridge and F.J. and L.F.C. from the UK Engineering and Physical Sciences Research Council (EPSRC). F.J. and L.F.C. acknowledge the support from the Henry Royce Institute made through EPSRC Grant No. EP/P02520X/1.

This work was supported in part by the Grant Agency of the Czech Republic under EXPRO Grant No. 19-28375X and by EU FET Open RIA under Grant No. 766566. CzechNanoLab project LM2018110 funded by the Ministry of Education, Youth and Sports of the Czech Republic is gratefully acknowledged for the financial support of the measurements and sample fabrication at LNSM Research Infrastructure.

The work of J.Z. was supported by the Ministry of Education, Youth and Sports of the Czech Republic from the OP RDE program under the project International Mobility of Researchers MSCAIF at CTU No. CZ.02.2.69/0.0/0.0/18 070/0010457 and through the e-INFRA CZ (ID:90140).

D.B. is grateful for support from a Leverhulme Trust Early Career Fellowship (No. ECF-2019-351) and a University of Glasgow Lord Kelvin Adam Smith Fellowship.

S.B. is supported by the DFG through project C08 of SFB 1143.

## AUTHOR DECLARATIONS

### Conflict of Interest

The authors have no conflicts to disclose.

### Author Contributions

**Johnson F.:** Conceptualization (lead); Data curation (lead); Formal analysis (lead); Investigation (equal); Methodology (equal); Software (equal); Visualization (lead); Writing – original draft (lead); Writing – review & editing (lead). **Kimák J.:** Conceptualization (equal lead); Data curation (lead); Investigation (lead); Methodology (lead); Writing – review & editing (equal lead). **Zemen J.:** Data curation (equal); Formal analysis (equal); Software (lead); Validation (lead); Writing – original draft (equal); Writing – review & editing (equal). **Šobáň Z.:** Investigation (equal); Methodology (equal). **Schmoranzerová E.:** Project administration (supporting); Supervision (equal); Writing – review & editing (equal). **Godinho J.:** Investigation (equal); Methodology (equal); Writing – review & editing (supporting). **Němec P.:** Funding acquisition (equal); Project administration (equal); Resources (equal); Supervision (equal). **Beckert S.:** Resources (equal); Validation (equal). **Reichlová H.:** Project administration (equal); Resources (equal); Supervision (equal). **Boldrin D.:** Validation (equal); Writing – review & editing (equal). **Wunderlich J.:** Conceptualization (equal); Supervision (equal). **Cohen L. F.:** Funding acquisition (lead); Project administration (lead); Supervision (lead); Writing – original draft (supporting); Writing – review & editing (equal).

## DATA AVAILABILITY

The data that support the findings of this study are available from the corresponding authors upon reasonable request.

## REFERENCES

[1]Y. Otani and T. Higo, "Domain structure and domain wall dynamics in topological chiral antiferromagnets from the viewpoint of magnetic octupole," Appl. Phys. Lett. **118**, 040501 (2021).
[2]S.-H. Yang, "Spintronics on chiral objects," Appl. Phys. Lett. **116**, 120502 (2020).
[3]D. Boldrin, A. P. Mihai, B. Zou, J. Zemen, R. Thompson, E. Ware, B. V. Neamtu, L. Ghivelder, B. Esser, D. W. McComb, P. Petrov, and L. F. Cohen, "Giant piezomagnetism in Mn3NiN," ACS Appl. Mater. Interfaces **10**, 18863–18868 (2018).
[4]D. Boldrin, I. Samathrakis, J. Zemen, A. Mihai, B. Zou, F. Johnson, B. D. Esser, D. W. McComb, P. K. Petrov, H. Zhang, and L. F. Cohen, "Anomalous Hall effect in noncollinear antiferromagnetic $Mn_3NiN$ thin films," Phys. Rev. Mater. **3**, 094409 (2019).
[5]F. Johnson, J. Zázvorka, L. Beran, D. Boldrin, L. F. Cohen, J. Zemen, and M. Veis, "Room temperature weak collinear ferrimagnet with symmetry driven, large intrinsic magneto-optic and magneto-transport signatures," arXiv:2111.13498 (2021).
[6]T. Nan, C. X. Quintela, J. Irwin, G. Gurung, D. F. Shao, J. Gibbons, N. Campbell, K. Song, S. Y. Choi, L. Guo, R. D. Johnson, P. Manuel, R. V. Chopdekar, I. Hallsteinsen, T. Tybell, P. J. Ryan, J. W. Kim, Y. Choi, P. G. Radaelli, D. C. Ralph, E. Y. Tsymbal, M. S. Rzchowski, and C. B. Eom, "Controlling spin current polarization through non-collinear antiferromagnetism," Nat. Commun. **11**, 4671 (2020).
[7]H. Reichlova, T. Janda, J. Godinho, A. Markou, D. Kriegner, R. Schlitz, J. Zelezny, Z. Soban, M. Bejarano, H. Schultheiss, P. Nemec, T. Jungwirth, C. Felser, J. Wunderlich, and S. T. B. Goennenwein, "Imaging and writing magnetic domains in the non-collinear antiferromagnet $Mn_3Sn$," Nat. Commun. **10**, 5459 (2019).
[8]T. Janda, J. Godinho, T. Ostatnicky, E. Pfitzner, G. Ulrich, A. Hoehl, S. Reimers, Z. Šobáň, T. Metzger, H. Reichlová, V. Novák, R. P. Campion, J. Heberle, P. Wadley, K. W. Edmonds, O. J. Amin, J. S. Chauhan, S. S. Dhesi, F. Maccherozzi, R. M. Otxoa, P. E. Roy, K. Olejník, P. Němec, T. Jungwirth, B. Kaestner, and J. Wunderlich, "Magneto-Seebeck microscopy of domain switching in collinear antiferromagnet CuMnAs," Phys. Rev. Mater. **4**, 094413 (2020).
[9]T. M. Tritt and M. A. Subramanian, "Thermoelectric materials, phenomena, and applications: A bird's eye view," MRS Bull. **31**, 188–198 (2006).
[10]F. J. DiSalvo, "Thermoelectric cooling and power generation," Science **285**, 703–706 (1999).

[11]A. V. Ettingshausen and W. Nernst, "Ueber das Auftreten electromotorischer Kräfte in Metallplatten, welche von einem Wärmestrome durchflossen werden und sich im magnetischen Felde befinden," Ann. Phys. **265**, 343–347 (1886).
[12]H. Chen, Q. Niu, and A. H. MacDonald, "Anomalous Hall effect arising from noncollinear antiferromagnetism," Phys. Rev. Lett. **112**, 017205 (2014).
[13]K.-I. Uchida, W. Zhou, and Y. Sakuraba, "Transverse thermoelectric generation using magnetic materials," Appl. Phys. Lett. **118**, 140504 (2021).
[14]T. Miyasato, N. Abe, T. Fujii, A. Asamitsu, S. Onoda, Y. Onose, N. Nagaosa, and Y. Tokura, "Crossover behavior of the anomalous Hall effect and anomalous Nernst effect in itinerant ferromagnets," Phys. Rev. Lett. **99**, 086602 (2007).
[15]S. N. Guin, K. Manna, J. Noky, S. J. Watzman, C. Fu, N. Kumar, W. Schnelle, C. Shekhar, Y. Sun, J. Gooth, and C. Felser, "Anomalous Nernst effect beyond the magnetization scaling relation in the ferromagnetic Heusler compound $Co_2MnGa$," NPG Asia Mater. **11**, 16 (2019).
[16]M. Ikhlas, T. Tomita, T. Koretsune, M.-T. Suzuki, D. Nishio-Hamane, R. Arita, Y. Otani, and S. Nakatsuji, "Large anomalous Nernst effect at room temperature in a chiral antiferromagnet," Nat. Phys. **13**, 1085–1090 (2017).
[17]X. Li, L. Xu, L. Ding, J. Wang, M. Shen, X. Lu, Z. Zhu, and K. Behnia, "Anomalous Nernst and Righi-Leduc effects in $Mn_3Sn$: Berry curvature and entropy flow," Phys. Rev. Lett. **119**, 056601 (2017).
[18]H. Narita, T. Higo, M. Ikhlas, S. Nakatsuji, and Y. Otani, "Effect of sample size on anomalous Nernst effect in chiral antiferromagnetic $Mn_3Sn$ devices," Appl. Phys. Lett. **116**, 072404 (2020).
[19]K. Kuroda, T. Tomita, M. T. Suzuki, C. Bareille, A. A. Nugroho, P. Goswami, M. Ochi, M. Ikhlas, M. Nakayama, S. Akebi, R. Noguchi, R. Ishii, N. Inami, K. Ono, H. Kumigashira, A. Varykhalov, T. Muro, T. Koretsune, R. Arita, S. Shin, T. Kondo, and S. Nakatsuji, "Evidence for magnetic Weyl fermions in a correlated metal," Nat. Mater. **16**, 1090–1095 (2017).
[20]J. He and T. M. Tritt, "Advances in thermoelectric materials research: Looking back and moving forward," Science **357**, 6358 (2017).
[21]C. Fu, Y. Sun, and C. Felser, "Topological thermoelectrics," APL Mater. **8**, 040913 (2020).
[22]J. Noky, J. Gooth, C. Felser, and Y. Sun, "Characterization of topological band structures away from the Fermi level by the anomalous Nernst effect," Phys. Rev. B **98**, 241106 (2018).
[23]S. Isogami, K. Masuda, Y. Miura, N. Rajamanickam, and Y. Sakuraba, "Anomalous Hall and Nernst effects in ferrimagnetic $Mn_4N$ films: Possible interpretations and prospects for enhancement," Appl. Phys. Lett. **118**, 092407 (2021).
[24]W. Zhou, K. Masuda, and Y. Sakuraba, "Origin of negative anomalous Nernst thermopower in Mn-Ga ordered alloys," Appl. Phys. Lett. **118**, 152406 (2021).
[25]D. Boldrin, E. Mendive-Tapia, J. Zemen, J. B. Staunton, A. M. Gomes, L. Ghivelder, J. Halpin, A. S. Gibbs, A. Aznar, J.-L. Tamarit, P. Lloveras, X. Moya, and L. F. Cohen, "Barocaloric properties of quaternary $Mn_3(Zn,In)N$ for room-temperature refrigeration applications," Phys. Rev. B **104**, 134101 (2021).
[26]X. Zhou, J.-P. Hanke, W. Feng, S. Blügel, Y. Mokrousov, and Y. Yao, "Giant anomalous Nernst effect in noncollinear antiferromagnetic Mn-based antiperovskite nitrides," Phys. Rev. Mater. **4**, 024408 (2020).
[27]F. Johnson, D. Boldrin, J. Zemen, D. Pesquera, J. Kim, X. Moya, H. Zhang, H. K. Singh, I. Samathrakis, and L. F. Cohen, "Strain dependence of Berry-phase-induced anomalous Hall effect in the non-collinear antiferromagnet $Mn_3NiN$," Appl. Phys. Lett. **119**, 222401 (2021).
[28]D. Xiao, Y. Yao, Z. Fang, and Q. Niu, "Berry-phase effect in anomalous thermoelectric transport," Phys. Rev. Lett. **97**, 026603 (2006).
[29]N. F. Mott and H. Jones, *The Theory of the Properties of Metals and Alloys* (Dover Publications, New York, 1958).
[30]Y. Pu, D. Chiba, F. Matsukura, H. Ohno, and J. Shi, "Mott relation for anomalous Hall and Nernst effects in $Ga_{1-x}Mn_xAs$ ferromagnetic semiconductors," Phys. Rev. Lett. **101**, 117208 (2008).
[31]T. Nomoto and R. Arita, "Cluster multipole dynamics in noncollinear antiferromagnets," JPS Conf. Proc. **30**, 011190 (2020).
[32]J. Železný, see https://bitbucket.org/zeleznyj/linear-response-symmetry for details about how to install and run the program for symmetry analysis.
[33]M. J. Grzybowski, P. Wadley, K. W. Edmonds, R. Beardsley, V. Hills, R. P. Campion, B. L. Gallagher, J. S. Chauhan, V. Novak, T. Jungwirth, F. Maccherozzi, and S. S. Dhesi, "Imaging current-induced switching of antiferromagnetic domains in CuMnAs," Phys. Rev. Lett. **118**, 057701 (2017).
[34]I. Gross, W. Akhtar, V. Garcia, L. J. Martínez, S. Chouaieb, K. Garcia, C. Carrétéro, A. Barthélémy, P. Appel, P. Maletinsky, J. V. Kim, J. Y. Chauleau, N. Jaouen, M. Viret, M. Bibes, S. Fusil, and V. Jacques, "Real-space imaging of non-collinear antiferromagnetic order with a single-spin magnetometer," Nature **549**, 252–256 (2017).
[35]T. Higo, H. Man, D. B. Gopman, L. Wu, T. Koretsune, O. M. J. van't Erve, Y. P. Kabanov, D. Rees, Y. Li, M.-T. Suzuki, S. Patankar, M. Ikhlas, C. L. Chien, R. Arita, R. D. Shull, J. Orenstein, and S. Nakatsuji, "Large magneto-optical Kerr effect and imaging of magnetic octupole domains in an antiferromagnetic metal," Nat Photonics **12**, 73–78 (2018).
[36]S. Sugimoto, Y. Nakatani, Y. Yamane, M. Ikhlas, K. Kondou, M. Kimata, T. Tomita, S. Nakatsuji, and Y. Otani, "Electrical nucleation, displacement, and detection of antiferromagnetic domain walls in the chiral antiferromagnet $Mn_3Sn$," Commun. Phys. **3**, 111 (2020).
[37]Y. Yamane, O. Gomonay, and J. Sinova, "Dynamics of noncollinear antiferromagnetic textures driven by spin current injection," Phys. Rev. B **100**, 054415 (2019).
[38]D. Fruchart, E. F. Bertaut, R. Madar, G. Lorthioir, and R. Fruchart, Solid State Commun. **9**, 1793 (1971).
[39]D. Boldrin, F. Johnson, R. Thompson, A. P. Mihai, B. Zou, J. Zemen, J. Griffiths, P. Gubeljak, K. L. Ormandy, P. Manuel, D. D. Khalyavin, B. Ouladdiaf, N. Qureshi, P. Petrov, W. Branford, and L. F. Cohen, "The biaxial strain dependence of magnetic order in spin frustrated $Mn_3NiN$ thin films," Adv. Funct. Mater. **29**, 1902502 (2019).
[40]I. Samathrakis and H. Zhang, "Tailoring the anomalous Hall effect in the noncollinear antiperovskite $Mn_3GaN$," Phys. Rev. B **101**, 214423 (2020).
[41]K. Momma and F. Izumi, "VESTA 3 for three-dimensional visualization of crystal, volumetric and morphology data," J. Appl. Crystallogr. **44**, 1272–1276 (2011).